Coordination of Frequency Reserves in an Isolated Industrial Grid Equipped with Energy Storage and Dominated by Constant Power Loads

Daniel dos Santos Mota, *Member, IEEE*, Erick Fernando Alves, *Senior Member, IEEE*, Salvatore D'Arco, Santiago Sanchez-Acevedo, and Elisabetta Tedeschi, *Senior Member, IEEE.*

***Abstract*—This paper examines the use of interconnected synchronous system requirements for frequency containment reserves (FCR) on isolated industrial grids that use turbogenerators as main source of energy, have high penetration of wind energy, are equipped with energy storage, and have a high level of constant power loads coupled by power electronic converters. Leveraging on the recent Nordic requirements for reserves in islanded operation (FCR_I), we propose an expansion that allows prioritizing among various reserve providers accounting for different isolated grid conditions. The study case of a complex, isolated industrial grid is selected to test this approach. The stability of this grid is evaluated via eigenvalues and participation factors considering the detrimental effects of constant power loads. It is demonstrated that, by prioritizing the reserve allocation to the faster converter-interfaced storage devices and loads, the overall stability is increased in addition to allowing the turbogenerators to operate at a more constant load. The results are supported by computer simulations of the complex isolated grid in DIgSILENT PowerFactory and by laboratory power-hardware-in-the-loop tests which compare the performance of the proposed concept with the industry consolidated droop control. The computer simulation models developed for this paper are made publicly available for reproducibility purposes.**

***Index Terms*—power system control, frequency control, industrial power system control, energy storage, stability, dc-ac power conversion**

NOMENCLATURE

BTC	Battery converter.
BTL	Battery main reactor.
CIL	Converter-interfaced load.
CPL	Constant power load.
CPS	Constant power source.
CZL	Constant impedance load.
EL	Electrolyzer.
ELC	Electrolyzer converter.
ESD	Energy storage device.
ESS	Energy storage system.
ESSGC	Energy storage system grid converter.
FC	Fuel cell.
FCC	Fuel cell converter.
FCR	Frequency containment reserves.
FCR_D	Large disturbance FCR.
FCR_I	Isolated operation FCR.
FCR_N	Normal operation FCR.
FLX	Flexible loads.
FLXGC	Flexible loads grid converter.
GC	Grid converter.
GHG	Greenhouse gas.
GT	Gas turbines or turbogenerator.
LPF	Low-pass filter.
NO_x	Nitrogen oxides.
O&G	Oil and gas.
PEC	Power electronic converter.
PEM	Proton exchange membrane.
PHIL	Power-hardware-in-the-loop.
PI	Proportional and integral.
PLL	Phase-locked loop.
PMS	Power management system.
PV	Photo-voltaic.
RES	Renewable energy source.
RTS	Real-time system.
TSO	Transmission system operator.
VSM	Virtual synchronous machine.
WF	Wind farm.
WT	Wind turbine.
WTGC	Wind turbine grid converter.

D. Mota and E. Alves were with the Department of Electric Power Engineering, Norwegian University of Science and Technology (NTNU), Trondheim, Norway at the time of first the manuscript submission. They are now with SINTEF Energy AS, Trondheim, Norway and with Hystar AS, Høvik, Norway, respectively.

S. D'Arco and S. Sanchez-Acevedo are with SINTEF Energy AS, Trondheim, Norway.

E. Tedeschi is with the Department of Electric Power Engineering, Norwegian University of Science and Technology (NTNU), Trondheim, Norway and with the Department of Industrial Engineering, University of Trento, Trento, Italy.

I. INTRODUCTION

THE petroleum sector is responsible for a considerable amount of the total greenhouse gas (GHG) emissions in many countries and is, simultaneously, one of the foundations of their socio-economic development. For instance, approximately $20\,\%$ of the total GHG emissions of Norway come from single-cycle gas turbines in operation in the oil and gas (O&G) fields in the Norwegian Continental Shelf [1]. Considerable emissions from the offshore O&G sector are also observed in other nations as the United Kingdom [2] and the Netherlands [3]. As part of the effort to reduce such emissions, a floating wind farm (WF) with eleven wind turbines (WTs) connected to two O&G platforms isolated from the continent [4] has recently been put in operation on the North Sea [5]. Such isolated industrial system presents

several challenges in the design, control and operation, as for example, constant power load-induced instabilities or the effects of active power imbalances. These phenomena need to be addressed from the early design stage by possibly adapting the control of generation units and by best exploiting existing assets. The challenges of balancing excess or underproduction from wind power in isolated O&G platforms have been identified and assessed in [6]–[8]. For mitigating wind variability in offshore applications, energy storage systems (ESSs), both centralized [9]–[11] and distributed [12], have been investigated in the literature. The operation of the platform's water injection system [13] as a flexible load in conjunction with wind power has, for instance, been assessed by [14]–[16].

Two critical operational aspects are the frequency control and the continuous compensation of imbalances between consumption and generation. These are normally counteracted by the activation of distributed power reserves in a hierarchic manner. Primary reserves perform a droop-based frequency control responding automatically after power imbalances and limiting frequency deviations in a time scale of seconds. Secondary reserves are subordinated to the grid's automatic generation control, which brings the frequency back to its rated value within seconds to minutes after power imbalances [17]. In the European context, primary reserves are named frequency containment reserves (FCR) and are coordinated nationally by transmission system operators (TSOs) [18].

Three types of FCR have recently been defined for the Nordic synchronous area, which includes the power grids of Finland, Sweden, Norway, and eastern Denmark. These types are [19]: normal operation frequency containment reserves (FCR_N), large disturbance frequency containment reserves (FCR_D), and islanded operation frequency containment reserves (FCR_I). FCR_N and FCR_D cooperate in the interconnected system, whereas FCR_I are a simplified version of the pair FCR_{N+D} that are activated only during islanding events. The same provider can supply any of these reserves, depending on the fulfillment of technical requirements, which are evaluated in a qualification process, and the grid operating conditions. Markets under the responsibility of the national TSOs are expected to be established for coordinating the availability and provision of these three types of FCR in the Nordic synchronous area [20]–[22].

Only the FCR_N are active when the grid frequency is within a given band around the rated value. If the frequency goes outside this band, the FCR_N saturate and the FCR_D are activated. This frequency band is common to the whole grid and is defined by the TSO. When in interconnected mode, an FCR provider may feature two different slopes in its power-frequency droop characteristic, namely, one for operation as FCR_N and another one for operation as FCR_D [19]. For larger frequency variations or in case of large rates of change of frequency, both criteria being defined by the TSO, a primary reserve provider must switch to the FCR_I mode. In this mode, the reserve provider adopts a single slope for its power-frequency droop characteristic [23].

Offshore isolated industrial grids typically employ one of three strategies for active power sharing between power generators [24]–[27]: 1) all units operate in isochronous mode, 2) one unit operates in isochronous mode while all others operate in droop control, and 3) all units operate in droop control with a centralized secondary frequency controller located in the grid's power management system (PMS). The first strategy demands a fast communication link among the generators implemented via an analog hardwired line or via serial communication. In case of faults in this communication line, the system defaults to the strategies with droop control which are analogous to the FCR_I operation defined for the Nordic synchronous area. It is worth noting that, despite operating in an analogous manner to FCR_I, the generators in isolated offshore installations are not required to fulfil grid codes defined by TSOs.

In this paper, an expansion of the Nordic synchronous area FCR_I concept is proposed together with a theoretical framework for the analysis of the distribution of reserves among multiple providers. The single slope power-frequency droop of the original FCR_I is expanded into a segmented droop with different regions for normal and for large disturbance operation. To the best extent of the authors' knowledge, the expanded FCR_I concept has not been explored in the offshore industry [24]–[26]. It has neither been investigated in the literature of isolated offshore O&G platforms expected to be connected to WFs with the support of ESSs [10], [11], [28], without the support of ESSs [7], [8], [29], [30], nor with inertial support provided by the WTs [8]. Moreover, the extended FCR_I concept was not employed in studies on the stability of power-intensive land-based isolated grids fed by hydro, diesel, and coal-based traditional synchronous generation that have to balance the intermittency of a considerable wind or photovoltaic (PV) contribution [31], [32] and it was not employed in the literature of ac microgrids [33]–[35] either.

This paper analyzes the stability and performance improvement due to the coordinated distribution of primary power reserves based on the expanded FCR_I concept in a relevant case study representative of an O&G installation, using numerical simulations in DIgSILENT PowerFactory 2020 SP2A and experimental validation. The impact of different contributions of the traditional synchronous generators and converter-interfaced devices controlling the grid frequency in the eigenvalues of the system is assessed first. Then, the paper presents experimental results obtained with real-time system (RTS) and power-hardware-in-the-loop (PHIL) tests which proved to be efficient tools for analysis and validation of devices and their controls in isolated grids [36]. As demonstrated in Section VII, when compared to the traditional droop control employed in the offshore O&G industry, the expanded FCR_I provides better performance especially in regard to frequency regulation and nadir.

The main contributions of this paper are: (1) It presents an expansion of the Nordic concept of FCR_I and demonstrates with numerical simulations and experimental tests the advantages, from a frequency control perspective, of replacing slower turbogenerators (GTs) by faster converter-interfaced ESSs as the main providers of primary power reserves. Moreover, it shows that this replacement causes a non-critical reduction in the damping of oscillation modes associated with frequency measurement transducers and controllers of constant

power devices. (2) It takes into consideration the negative effects caused by constant power loads (CPLs) in the electrical grid, an issue commonly overlooked in the literature of power-intensive isolated grids. (3) It performs a comparison with an industry state-of-the-art control strategy that provides valuable insights for the application of the extended FCR_I in increasingly complex islanding scenarios in interconnected systems with traditional synchronous generation, large participation of intermittent renewable energy sources (RESs), and ESSs.

The paper is organized as follows: the expanded FCR_I concept and the issues caused by CPLs are presented in Section II, the sharing and the coordination of power reserves in an isolated grid are explained in Section III, a theoretical approach for the expanded FCR_I concept via modeling and stability analysis is performed in Section IV, the study case is introduced in Section V, a validation of the theoretical analysis is presented in two sections with a detailed stability assessment in Section VI and an experimental validation with laboratory PHIL tests in Section VII, a comparison between the proposed concept and an offshore industry state-of-the-art control strategy is performed in Section VIII, a discussion is made in Section IX, and, finally, the concluding remarks are listed on Section X.

II. Frequency Containment Reserves for Operation in Isolated Grids Dominated by Constant Power Loads

A. Frequency Containment Reserves for Isolated Operation

Large interconnected systems and isolated grids have to face the challenges brought by an increased penetration of intermittent RESs. In the Nordic synchronous area, primary reserve providers are required to have two parameter sets, one for island operation and another one for interconnected operation. In case of an islanding event, the reserve provider must switch to the FCR_I mode and adopt a single slope for its power-frequency droop characteristic [23], as illustrated in Fig. 1. Within this context, an expansion of the single-slope power-frequency droop characteristic of the Nordic FCR_I concept into a segmented one with different regions for normal and large disturbance operation is proposed in this paper, see Fig. 2. This expanded concept is applied to a study case representing an O&G platform connected to a WF and equipped with an ESS. For simplicity of notation, the normal isolated operation reserves are named FCR_N and the large disturbance reserves for isolated operation are named FCR_D. These new FCR_N and FCR_D for isolated grids are analogous to the ones for interconnected operation defined in [19].

The expanded FCR_I characteristic of the system is illustrated by Fig. 2. The limit $\widetilde{f}_\text{N}$ between the regions of FCR_N and FCR_D activation is defined in terms of the deviation of the measured ac frequency $\widehat{f}$ from its nominal value f_n, namely $\widetilde{f} = \widehat{f} - f_\text{n}$. FCR_N are active and FCR_D are inactive when the $|\widetilde{f}| \leq \widetilde{f}_\text{N}$. The value of $\widetilde{f}_\text{N}$ is $0.1\,\text{Hz}$ ($0.2\,\%$) for the Nordic interconnected grid [19]. However, isolated grids usually have to endure more severe relative power imbalances and resulting frequency disturbances than a country or continental wide grid. For instance, the recommended practices for the design of electrical power generation in merchant, commercial, and naval

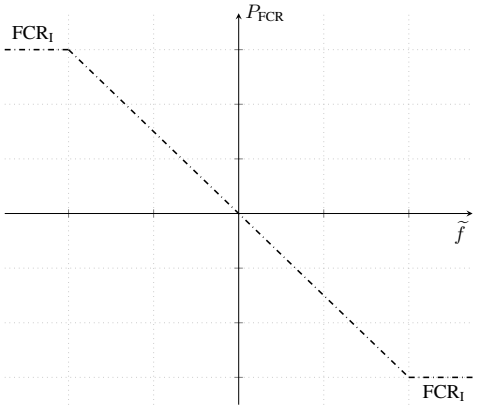

Fig. 1: Original FCR_I characteristic [23].

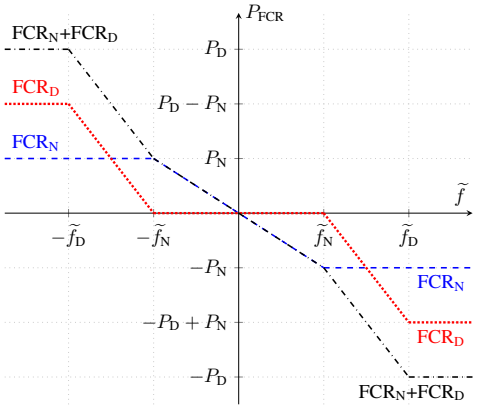

Fig. 2: Proposed expanded FCR_I characteristic of the system, adapted from the $\text{FCR}_\text{N+D}$ for interconnected operation defined by [19].

vessels [37] define a tolerance of $\pm 3\,\%$ for the "maximum permitted departure from nominal frequency during normal operation, excluding transient and cyclic frequency variations." Hence, a value between $0.2\,\%$ and $3\,\%$ will later be adopted for $\widetilde{f}_\text{N}$ in Sections VII and VIII. The system is considered under a large disturbance when $|\widetilde{f}| > \widetilde{f}_\text{N}$. In this condition, the FCR_N are saturated at P_N and the FCR_D are activated.

B. Constant Power Loads

WTs as well as solar PV panels can be considered constant power sources (CPSs) as their controllers typically operate in maximum power point tracking, in other words, tracking the optimum power for a given wind speed or solar irradiation [38]. Storage devices connected to a common ESS dc link, as the ones studied in [9], [10], can also run as CPLs or CPSs. Isolated industrial grids can, moreover, serve a considerable amount of CPLs such as variable frequency drives [13], [39].

Even though constant power loads and sources are known to cause instabilities in dc microgrids [40], [41] and in ac microgrids [42], [43], it is common in studies of the integration of wind power supported by ESSs and by converter-interfaced flexible loads (FLX) [9], [10], [14], as well as only supported by an ESS [11], [28], to represent the total electrical load of the isolated O&G platform as constant impedance loads (CZLs).

Power electronic oriented studies on CPLs in microgrids [44], [45], moreover, tend to focus on the stability of the converters, not in frequency control nor in the stability of the complete grid. If combined with power electronic converters (PECs), CPL and CPS also give rise to new instability phenomena both in micro and in large interconnected grids [36], [46]. Remark that modern type 4 [47] WTs, solar PV farms, ESSs, and some types of loads are all connected to the grid via full-power PECs. Converter driven instabilities, therefore, should not be overlooked when integrating this equipment in isolated grids.

III. Sharing and Coordination of Primary and Secondary Reserves

The stochastic nature of wind can lead to an increased number of start-stop operations and more variable load profiles for the GTs of an O&G platform connected to a WF resulting in higher wear and tear, unintended higher nitrogen oxides (NO_x) emissions, and an overall degradation of the electric power quality and grid frequency stability [48], [49]. Therefore, coordination strategies that allow prioritizing converter-interfaced loads (CILs) and ESS instead of GTs as the main source of power for fast frequency control are key to a successful integration of wind power into offshore O&G facilities. In this section, a hierarchic frequency control structure that allows such prioritization and employs the extended FCR_I concept is explained.

A. Secondary Reserves

Fig. 3 depicts the frequency control structure of the study case's autonomous grid where reserve providers play a subordinate role under a centralized PMS. The secondary frequency controller, which is a part of the PMS, is responsible for correcting steady-state errors in the frequency of the isolated grid. It employs a proportional and integral (PI) regulator that reacts to the frequency deviation and generates the total secondary power reference $\overset{*}{P}_\text{S}$ which is shared among two GTs and a pair of fuel cell (FC) and electrolyzer (EL). The measured and filtered value of the power delivered by the FC and EL, denoted by $\widehat{P}_\text{FC}$ and $\widehat{P}_\text{EL}$, respectively, are deducted from the secondary power reference sent to the governors of the GTs, see (1). Although not represented in Fig. 3, the reserve providers have their own limits for rate of change of power and the GTs have an extra input for the base load power reference.

$$P_\text{S}^{*\text{EL}} = P_\text{S}^{*\text{FC}} = \overset{*}{P}_\text{S}, \quad P_\text{S}^{*\text{GT1}} = P_\text{S}^{*\text{GT2}} = \frac{\overset{*}{P}_\text{S} - \widehat{P}_\text{FC} - \widehat{P}_\text{EL}}{2} \tag{1}$$

B. Primary Reserves

The distributed primary frequency control is performed locally at each reserve provider. All FCR_N providers shall be able to supply their allocated reserve power P_N for a frequency drop of $\widetilde{f}_\text{N}$. Conversely, the providers should absorb P_N for a

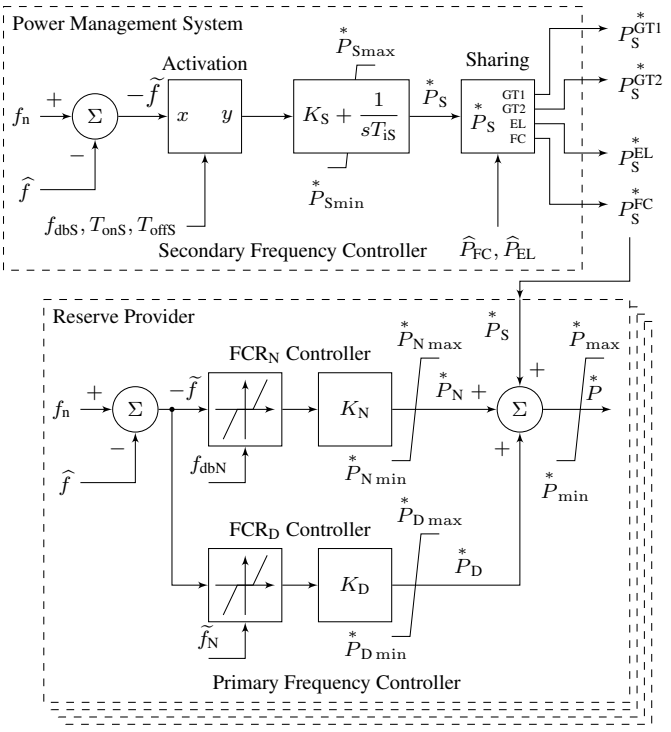

Fig. 3: Hierarchic structure of the ac frequency control.

frequency increase of $\widetilde{f}_\text{N}$. Therefore, the frequency-to-power gain of a FCR_N provider is

$$K_\text{N} = \frac{P_\text{N}}{\widetilde{f}_\text{N}} \ [\text{W/Hz}]\,. \tag{2}$$

When considered for the whole system, this gain is called regulating strength in [19] and frequency bias in [17]. In this paper, it will be referred to as FCR gain or as frequency-to-power gain. The FCR_D frequency-to-power gain is defined as

$$K_\text{D} = \frac{P_\text{D} - P_\text{N}}{\widetilde{f}_\text{D} - \widetilde{f}_\text{N}} \ [\text{W/Hz}]\,. \tag{3}$$

The total frequency-to-power characteristic of the system is, therefore, a composition of the normal and large disturbance reserves as illustrated in Fig. 2. The FCR_D controllers feature a dead band between $\pm\widetilde{f}_\text{N}$ which ensures that only the FCR_N are activated in normal operation, as shown in Fig. 3. Notice that gains K_N and K_D do not necessarily have to be equal. It is also worth reminding that the FCR_N are saturated at P_N and the FCR_D are activated when $|\widetilde{f}| > \widetilde{f}_\text{N}$.

C. FCR Controllers

The power contribution of the FCR providers is a function of $\widetilde{f}$. Each provider measures the ac frequency $\widehat{f}$ and subtracts it from the rated frequency f_n, see Fig. 3. The resulting $-\widetilde{f}$ is fed to two proportional controllers, one for FCR_N and one for FCR_D. Each controller has its own gain (K), limiters ($\max$, $\min$), and a symmetric dead band (f_dbN and $\widetilde{f}_\text{N}$). The FCR_N power reference ($\overset{*}{P}_\text{N}$) and the FCR_D power reference ($\overset{*}{P}_\text{D}$) are summed to the secondary power reference ($\overset{*}{P}_\text{S}$), which is given to the providers by the PMS via communication link. The total

power reference output ($\overset{*}{P}$) has its own independent maximum and minimum limits.

The PMS allocates a primary reserve quota to each provider based on a security assessment, which takes into consideration the grid operational conditions and the forecasts of loads and RES. To receive a quota, the provider must be able to respond symmetrically to both positive and negative variations in $\widetilde{f}$ and deliver the total assigned reserve power P_{N} (up or down) when $|\widetilde{f}| = \widetilde{f}_{\mathrm{N}}$. Based on the assigned reserves, each provider calculates its gains K_{N} and K_{D} according to (2) and (3), respectively. Remark that the transient response of each FCR provider does not rely on a fast communication link with the PMS, as the FCR control loops are implemented locally and fast dynamic changes to the power allocation are not expected.

D. Role of Dead Bands in FCR

The normal operation and large disturbance reserves are properly coordinated by a dead-band block in the $\mathrm{FCR_D}$ providers, shown in Fig. 3. The limit frequency $\widetilde{f}_{\mathrm{N}}$ is unique for the system and is known by all FCR providers. By adjusting the $\mathrm{FCR_D}$ dead band to $\widetilde{f}_{\mathrm{N}}$, one guarantees that the large disturbance reserves will only be activated once the $\mathrm{FCR_N}$ are saturated. The limits $\overset{*}{P}_{\mathrm{N\,max}}$ and $\overset{*}{P}_{\mathrm{N\,min}}$ of each $\mathrm{FCR_N}$ provider are assumed to be symmetric and their absolute values are equal to P_{N}. Although not a desirable feature, a non negligible dead band f_{dbN} might be necessary for a proper operation of a specific $\mathrm{FCR_N}$ provider. In this case, calculating the gain K_{N} with (2) leads to a reduced $\mathrm{FCR_N}$ capacity. If the provider requires a small dead band for proper operation, the effects of the dead band can be compensated locally by calculating the frequency-to-power gain according to (4) without the intervention of the PMS.

$$K_{\mathrm{N}} = \frac{P_{\mathrm{N}}}{\widetilde{f}_{\mathrm{N}} - f_{\mathrm{dbN}}} \tag{4}$$

IV. Stability Assessment with a Rotating Mass Model

Converter interfaced reserves have much faster responses than traditional turbogenerators [50]. The benefits of these faster responses can be evaluated, initially, with the classical rotating mass model [51], [52]. For that, the spinning reserves of the system (the GTs) are aggregated into a single rotating mass with moment of inertia J. The turbines apply torque to increase the angular frequency ω of the rotating mass, whereas the aggregated electrical loads apply torque to reduce ω. When expressed in terms of power, the balance of torque of this simplified model is

$$\omega J \frac{\mathrm{d}\omega}{\mathrm{d}t} = P_{\mathrm{FCR}} + P_{\mathrm{S}} - P_{\mathrm{L}} \tag{5}$$

where $\omega = 2\pi f$, P_{FCR} is the power supplied by the FCR, P_{S} is the secondary frequency control power, and P_{L} is the total electric load power.

Let the following variables be introduced:

$$H = J\frac{\omega_{\mathrm{n}}^2}{2S_{\mathrm{n}}},\ \widetilde{p}_{\mathrm{FCR}} = \frac{P_{\mathrm{FCR}}}{S_{\mathrm{n}}},\ \widetilde{p} = \frac{P_{\mathrm{L}} - P_{\mathrm{S}}}{S_{\mathrm{n}}},\ \widetilde{\mathtt{f}} = \frac{\omega - \omega_{\mathrm{n}}}{\omega_{\mathrm{n}}} \tag{6}$$

where H is the inertia constant of the spinning reserves, ω_{n} is the nominal angular frequency, S_{n} is the base power of the isolated grid, $\widetilde{p}_{\mathrm{FCR}}$ is the normalized power supplied by the FCR, $\widetilde{p}$ is the normalized imbalance of power between load and secondary reserves, and $\widetilde{\mathtt{f}}$ is the normalized deviation of the system frequency.

By using the variables in (6) and assuming $\omega \approx \omega_{\mathrm{n}}$, (5) can be re-written in the Laplace domain as (7), where s is the complex angular frequency. The FCR provider features a proportional controller and actuator that react to deviations in the system frequency. In the Laplace domain, the FCR power response can be represented in a simplified way as in (8), where $k = K\omega_{\mathrm{n}}/S_{\mathrm{n}}$ is the normalized FCR gain and the delay introduced by the actuator is modeled by a first-order low-pass filter (LPF) with a time constant T. From (7) and (8), it is possible to obtain the transfer function $G(s)$ between $\widetilde{p}$ and $\widetilde{\mathtt{f}}$, as show in (9).

$$2H\widetilde{\mathtt{f}}s = \widetilde{p}_{\mathrm{FCR}} - \widetilde{p} \tag{7}$$

$$\widetilde{p}_{\mathrm{FCR}} = -\frac{k}{sT+1}\ \widetilde{\mathtt{f}} \tag{8}$$

$$G(s) = \frac{\widetilde{\mathtt{f}}(s)}{\widetilde{p}(s)} = -\frac{sT+1}{2HTs^2 + 2Hs + k} \tag{9}$$

A constant imbalance of power $\widetilde{p}$ causes a steady-state variation in the system frequency that is inversely proportional to the gain k. It is important to emphasize that the inertia constant H does not influence the steady-state error. However, H, T, and k play a role in how fast and how smoothly $\widetilde{\mathtt{f}}$ reaches the steady-state after a power imbalance. The damping ζ and the natural frequency of the system ω_{nat}, which can be calculated by algebraic manipulation of (9), are a function of H, k, and T, as shown in (10). The higher the inertia constant, the more stable the system is. The longer the delay T, the more oscillatory the system is and the slower ω_{nat} becomes.

$$\zeta = \sqrt{\frac{H}{2kT}}\ , \quad \omega_{\mathrm{nat}} = \sqrt{\frac{k}{2HT}} \tag{10}$$

The FCR control strategy adopted in this paper does not include, on purpose, virtual synchronous machines (VSMs) nor terms with the time derivative of the frequency. The reasons for that are: 1) the equivalence between frequency droop and VSMs has been pointed out by [53]; 2) enough physical inertia is available in the study case presented in Section V due to the GTs; 3) the time delay T of the actuator controlling the primary reserve power has a considerable impact on the damping of oscillations in the system frequency, as indicated by the second order transfer function $G(s)$ in (9) and by ζ in (10). The longer the delay of the actuator, the more oscillatory the system becomes. As it will be demonstrated in this paper, the primary frequency reserves provided by a fast ESS improve the stability of the system even without the use of VSMs.

When the primary reserve is provided by traditional GTs, the total intrinsic delay of the governor and turbine is in the order of hundreds of milliseconds [54]. However, if the primary reserve is provided by an ESS, the delay drops by at least one order of magnitude [50]. When T in (9) approaches

zero, the transfer function between the power imbalance and the system frequency tends to a first-order low-pass filter. For the normal operation of an isolated grid, a two-fold advantage is obtained by allocating the FCR_N to the ESS and leaving the GTs only with FCR_D. Firstly, the GTs are allowed to operate at a more constant power which reduces the wear and tear of the mechanical parts. Secondly, the system becomes less oscillatory even without a VSM scheme or derivative terms at the ESS reserves.

A. Multiple FCR Providers

The balance of power in (7) can be written as (11) for a system with n reserve providers that are modeled as first-order LPFs with gains k_i and delays T_i as in (8). The resulting transfer function $G(s)$ between $\widetilde{p}$ and $\widetilde{\mathtt{f}}$ becomes of order $n+1$, as shown in (12). A constant imbalance of power $\widetilde{p}$ causes a steady-state deviation in $\widetilde{\mathtt{f}}$ that is inversely proportional to the sum of gains k_1 to k_n and depends neither on the inertia constant nor on the providers' time delays, as demonstrated in (13) by the application of the final value theorem to $G(s)\widetilde{p}(s)$ when the unbalance $\widetilde{p}(s)$ is a step with amplitude p. However, H, delays T_i, and gains k_i concurrently affect the location in the complex plane of the poles of $G(s)$, in other words, they influence the damping and natural frequency of the system's oscillation modes. It is, nonetheless, important to remark that the linearized rotating mass model which results in (9) and (12) disregards the involved dynamics of the electrical grid. Although a thorough stability analysis demands a more sophisticated model, this simplified approach gives valuable insights on the roles of the system's inertia, gains, and time delays. The interested reader may find more information on conditions for robust frequency stability of power grids in [55].

$$2H\widetilde{\mathtt{f}}s = \widetilde{p}_\text{FCR} - \widetilde{p} = -\left(\sum_{i=1}^{n} \frac{k_i}{sT_i+1}\right)\widetilde{\mathtt{f}} - \widetilde{p} \tag{11}$$

$$G(s) = \frac{\widetilde{\mathtt{f}}(s)}{\widetilde{p}(s)} = \frac{-\prod_{i=1}^{n}(sT_i+1)}{\left(2Hs\prod_{i=1}^{n}(sT_i+1)\right) + \sum_{j=1}^{n}\left(k_j \prod_{i=1|i\neq j}^{n}(sT_i+1)\right)} \tag{12}$$

$$\lim_{t\to\infty}\widetilde{\mathtt{f}}(t) = \lim_{s\to 0} sG(s)\widetilde{p}(s) \xrightarrow{\widetilde{p}(s)=\frac{p}{s}} \lim_{t\to\infty}\widetilde{\mathtt{f}}(t) = \frac{-p}{\sum_{j=1}^{n} k_j} \tag{13}$$

B. Modal Analysis

It is interesting to assess the stability of the study case with the simplified model given by (11) when the FCR is shared between two GTs and the ESS. For that, the normalized $\widetilde{p}_\text{FCR}$ is split into three components, one for the ESS and two for the GTs. The ESS component is modeled as a first-order LPF. For the GTs, two first-order LPFs are used in series representing the fuel valve and turbine delays. The model data is shown in Table I. The total power-to-frequency gain of the FCR is set to $K_\text{N} = 12\,\text{MW/Hz}$ and is shared between the GTs and ESS. This gain is reasonably high when compared to the installed GT power of 88 MVA and the electric load of 44 MW. For large interconnected grids in North America, the typical gain in W/Hz is on the range of 10 % of the peak demand in W [17].

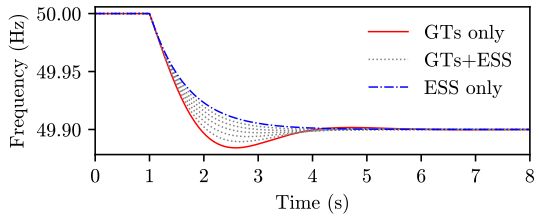

Fig. 4: Frequency during a step load of 1.2 MW with different sharing of FCR_N between ESS and GTs.

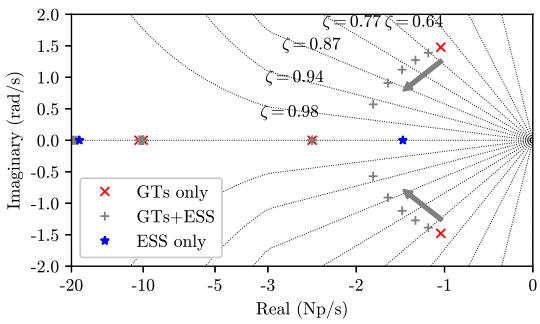

Fig. 5: Eigenvalues with linearized rotating mass model for a total gain of 12 MW/Hz and different sharing of FCR_N between ESS and GTs.

TABLE I: Simulation data for Figs. 4 and 5.

Parameter	Value
Total apparent power GTs	88 MVA
Electric load	44 MW
Total FCR gain	12 MW/Hz
System inertia constant	2.5 s
ESS time constant	50 ms
GTs fuel valve time constant	0.1 s
GTs turbine time constant	0.4 s

Figs. 4 and 5 show, respectively, the frequency after a step load of 1.2 MW and the eigenvalues of the system obtained with MATLAB Simulink R2018a for seven different FCR sharing configurations as listed on Table II. The model and dataset are available at [56]. The frequency nadir (the minimum value attained after the step) in Fig. 4 is greatly improved by shifting the primary reserves from the slower GTs to the faster converter-interfaced ESS. In Fig. 5, for all FCR configurations, the eigenvalues associated with the ESS are not oscillatory and lie on the real number axis. The governors are associated with the only oscillatory mode. When only the GTs are supplying FCR, this mode features a natural frequency of $\omega_\text{nat} = 1.651\,\text{rad/s}$ and a damping of $\zeta = 0.606$. These are the same ω_nat and ζ one would obtain with (10) if the GTs,

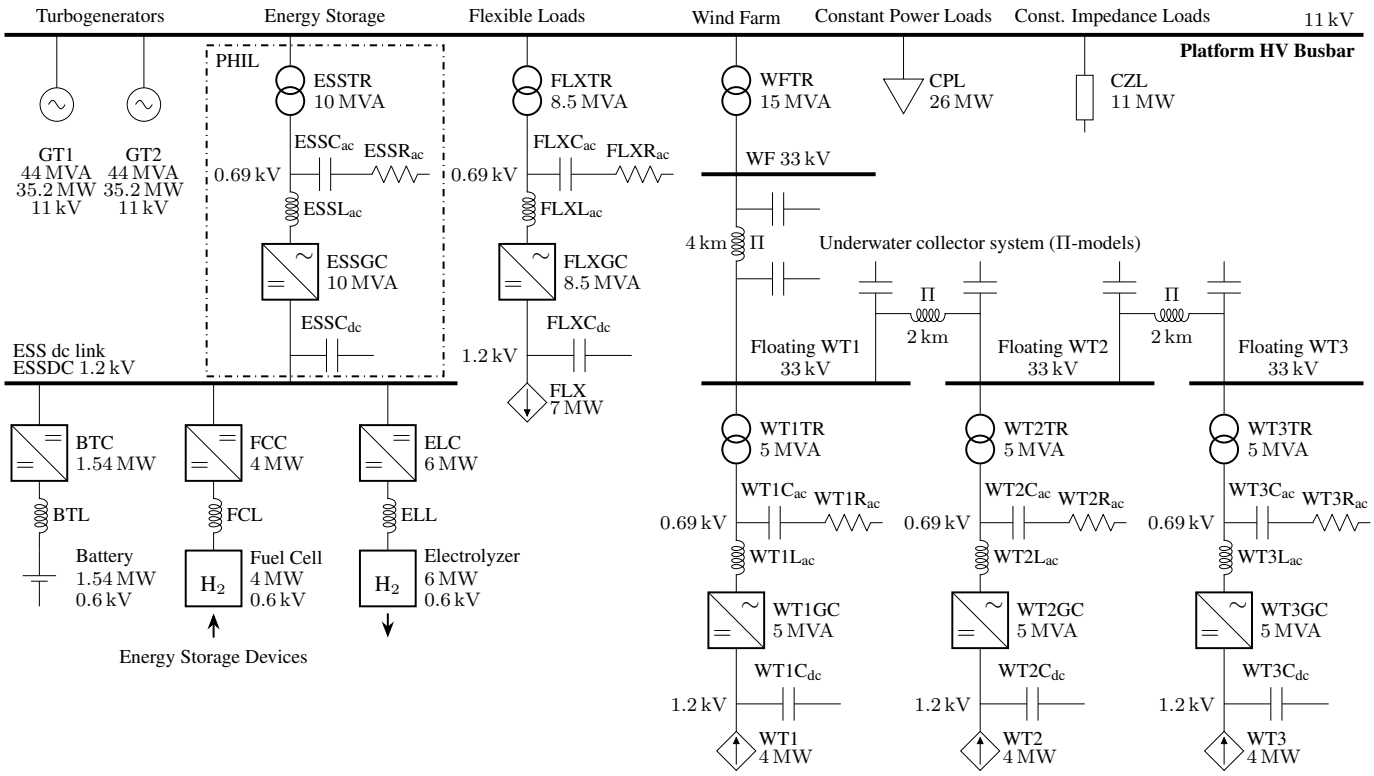

Fig. 6: Single line diagram of the study case.

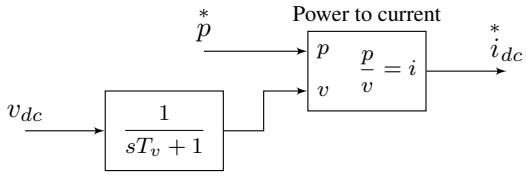

Fig. 7: Current reference calculation for the controlled current sources FLX, WT1, WT2, and WT3 in Fig. 6 that operate as CPL or CPS.

with gains and time constants in Table I, were aggregated into a single unit modeled with one first-order LPF. Notice, also, that the more the reserves shift towards the ESS, the more the oscillatory mode moves towards the real number line. When only the ESS provides FCR, the imaginary parts of all eigenvalues are zero.

V. Study case: An Isolated Industrial Grid

The study case used in this paper is based on an existing O&G platform in the North Sea. The platform operates isolated from the continent and is fed, in normal operation, by two $35.2\,\mathrm{MW}$ aero-derivative single-cycle GTs. A techno-economical study [49] suggested that a reduction of approximately $30\,\%$ of the annual CO_2 emissions can be achieved if the platform were connected to a $12\,\mathrm{MW}$ floating offshore WF. The reduction, however, relies on the installation of a centralized hybrid ESS with $4\,\mathrm{MW}$ proton exchange membrane (PEM) fuel cells and $6\,\mathrm{MW}$ PEM electrolyzers. A set of three $4\,\mathrm{MW}$ WTs was used by [9] as a prospective scenario for proposing a sizing methodology for the platform's hybrid ESS. This same scenario was also used by [10], [57]. Fig. 6 shows a single-line diagram of the study case. The average electrical load of the platform is $44\,\mathrm{MW}$. Each of the $35.2\,\mathrm{MW}$ GTs alone is not able to feed the platform. Additionally, the thermal load of the industrial processes [13] requires one of the GTs to be in operation at all times. Due to safety concerns, the prospective scenario investigated by [9], [10], [57] assumed that two GTs would still operate simultaneously even with full production from the WF. The premise of two GTs operating at all times is kept in this paper to allow the re-use of the aforementioned scenario.

The loads of the study case are divided into three groups in Fig. 6. The first group represents the platform's water injection system, whose variable frequency drives can act as flexible loads (FLX) and provide primary frequency control reserves. For simplification purposes, the whole water injection system is grouped under a single $8.5\,\mathrm{MVA}$ active-front-end PEC. The second load group aggregates $26\,\mathrm{MW}$ of CPL which are modeled as instantaneous constant power consumers, in other words, there are no delays associated to them. The third group gathers $11\,\mathrm{MW}$ of CZL. Both CPL and CZL can be changed in steps for testing the dynamic characteristics of the model.

The FLX are modeled as a single ideal controlled current source feeding a dc link. The current supplied by this controlled source depends on the power consumed by the flexible loads and on the dc-link voltage. Fig. 7 illustrates the calculation of the reference for the FLX controlled current source. The dc voltage measurement is modeled as a first order LPF with a time constant T_v. The flexible loads grid converter

(FLXGC) interfaces the dc link to the platform's ac grid. It operates as a dc voltage controller and, in addition to that, regulates the reactive power exchange with the grid to zero.

The WTs with their wind turbine grid converters (WTGCs) are modeled in a similar way to the flexible loads and FLXGC. The turbines including generator and machine side converter are simplified to a single controlled current source that supplies constant power even when the dc-link voltage varies. Fig. 7 illustrates the calculation of the references for the WT controlled current sources. Similarly to the FLXGC, the WTGCs operate as dc voltage controllers and regulate the reactive power exchange with the grid to zero. As the back-to-back PECs employed in modern type 4 WTs isolate the mechanical oscillation modes from the states on the electrical grid side [58], this simplified representation of the wind turbine units can be adopted.

For counteracting wind variability, a hybrid ESS is employed. A fast energy storage device (ESD) composed of a battery and a dc/dc converter provides reserves for the short term wind and load variations. The main goal of the battery is to reduce the burden of the GTs on the fast frequency control. The pair of electrolyzer and fuel cell form one single ESD. Energy is stored as hydrogen when there is wind overproduction and hydrogen is transformed into electricity when there is little production from the WF. Even though the reactive power provided by ESSs can have an important role in avoiding the loss of synchronism of nearby machines in the event of faults [59], the energy storage system grid converter (ESSGC) of the study case keeps the reactive power exchange with the grid equal to zero. Reactive power support from the ESSGC is going to be addressed in a future work. Similarly to the grid converters (GCs) of the FLX and WTs, the ESSGC also runs as a dc voltage controller. The choice of setting the GC as a dc voltage regulator while the ESDs provide power to the dc link has been previously addressed by [10], [60]. The PowerFactory models developed by [10], which are publicly available at [61], are used as base for this paper.

VI. Detailed Stability Assessment

The mechanical rotating mass model which results in the transfer functions (9) and (12) disregards many interactions between the devices of the platform. Therefore, CPL and converter-driven instabilities are not captured by these transfer functions. To gain an insight into these complex interactions and to validate the results of the simplified stability assessment presented in Section IV-B, computer simulations were performed with DIgSILENT PowerFactory 2020 SP2A. Due to brevity concerns, the consolidated tuning techniques in line with industrial and academic praxis employed for the various controllers in turbine governors, excitation systems, and PECs are not discussed in this paper. Nevertheless, the interested reader may find more information on electrical power systems in [51], [52], on the models employed in this paper in [62], on turbine governors in [54], on excitation systems in [63], on traditional tuning techniques for PI controllers in [64], and on the tuning of ac current and dc voltage regulators applied to PECs in [65]. It is important to remark that the models

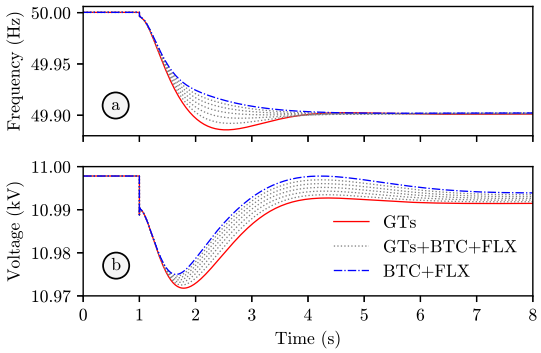

Fig. 8: Voltage and frequency at the main busbar during a step load of 1.2 MW.

TABLE II: FCR_N sharing values and chart information for Figs. 4, 5, 8 and 9.

Chart legends		GTs	GTs+BTC+FLX					BTC+FLX
GT1,2	K_N [MW/Hz]	6	5	4	3	2	1	0
BTC	K_N [MW/Hz]	0	1	2	3	4	5	6
FLX	K_N [MW/Hz]	0	1	2	3	4	5	6
Line style		———	·····					—·—
Marker		×	+					⋆

and datasets used for obtaining Figs. 5, 8 and 9 are available at [56].

Fig. 8a shows seven instances of frequency changes caused by a step load of 1.2 MW. The frequency shown is the one at the platform's main busbar measured with a phase-locked loop (PLL) [66]. The FCR_N sharing is different in each of the seven instances as listed on Table II. The step load is applied at $t = 1$ s. Within the next 4 s, the frequency reaches a new steady state at 49.9 Hz. The response when the GTs are the only FCR_N providers is shown in solid red. In this case, the minimum value reached by the frequency (known as nadir) is 49.886 Hz. The responses when the FCR_N are shared between GTs, battery converter (BTC), and FLX are shown in dotted gray. The dash dotted blue curve denotes the response when only BTC and FLX provide FCR_N. From a frequency control perspective, the system becomes more stable as the FCR_N contribution is shifted towards the BTC and FLX. These faster primary reserves improve the nadir. It is worth comparing the response in Fig. 8a to the one obtained with the simplified rotating mass model in Fig. 4. Although very similar, the detailed modeling with DIgSILENT PowerFactory 2020 SP2A shows that other complex interactions can destabilize the grid. The response of the main busbar voltage, for instance, becomes slightly less damped (Fig. 8b). The voltage control dynamics of the active front-end converters ESSGC and FLXGC should always be considered in a thorough stability analysis.

When the steady state is reached in the simulations shown in Fig. 8, the eigenvalues of the system are calculated together with the participation factors of each state in each eigenvalue. The result is shown in Fig. 9. See Table II for information regarding chart legend and markers. The devices whose internal states have a participation factor higher than 50 % are named on the side of some specific eigenvalues.

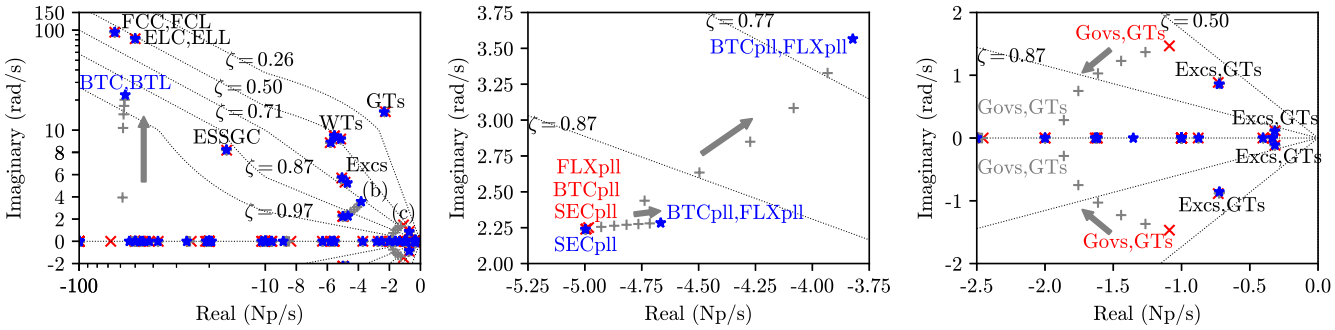

(a) Overview (b) Detail frequency measurement (c) Detail governors

Fig. 9: Complex plane with eigenvalues, for legend information see Table II.

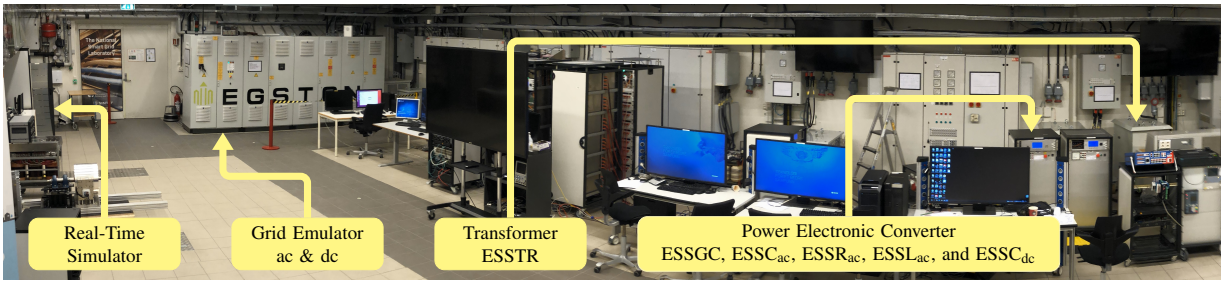

Fig. 10: PHIL setup at the National Smart Grid Laboratory.

The real and imaginary axes are partially linear and partially logarithmic in Fig. 9a. Both axes of Figs. 9b and 9c are linear. Constant damping (ζ) lines are plotted to help identifying the more oscillatory eigenvalues. The system is stable in all configurations and, as expected, all eigenvalues have negative real parts.

Fig. 9a shows an overview of the complex plane. The negative half of the imaginary axis is mostly omitted as oscillatory modes appear as complex conjugate eigenvalues. The eigenvalue related to the BTC and the battery main reactor (BTL) leave the real number line and reach a damping of $\zeta = 0.94$ with a natural frequency of $22\,\mathrm{rad/s}$ when the reserves are exclusively supplied by the BTC and FLX. The modes related to fuel cell converter (FCC) and fuel cell main reactor are marked with FCC,FCL and the ones related to the electrolyzer converter (ELC) and electrolyzer main reactor are marked with ELC,ELL. The eigenvalues related to the wind turbines including its converters are clustered together and are marked with WTs. The modes associated with the FCC, ELC, and WTs are not affected by the $\mathrm{FCR_N}$ sharing. They are, nevertheless, influenced by the tuning of the controllers of their PECs. However, due to brevity concerns, the influence of controller tuning in the location of these eigenvalues will not be investigated in this paper. It is worth noting, though, that FCC, ELC, WTs, and BTC operate as constant power devices. Other eigenvalues worth remarking are the ones associated with the excitation system of the turbogenerators (Excs), the ones related to the grid converter of the ESS (ESSGC), and the ones related to internal states of the turbogenerators (GTs).

Fig. 9b shows a detail of the complex plane with eigenvalues related to the frequency measurement (performed with PLLs) of the flexible loads (FLXpll), battery converter (BTCpll), and secondary frequency controller (SECpll). When the reserves are provided by the GTs only, three eigenvalues are clustered close to the point $-5 + j2.25$. Each of those eigenvalues is related to one frequency measurement device. Once the $\mathrm{FCR_N}$ is shifted from the GTs to the FLX and BTC, two eigenvalues start to move towards less damped regions of the complex plane. States of the PLLs of the BTC and FLX have a participation factor above $50\,\%$ in these eigenvalues. The eigenvalue related to the secondary frequency controller PLL, however, is not affected by the sharing of $\mathrm{FCR_N}$.

Fig. 9c presents a detailed view including the oscillation modes associated with the governors and turbogenerators (Govs,GTs). The dynamic of this mode coincides with the one observed in Fig. 5. As indicated by the gray + markers, the less the GTs provide $\mathrm{FCR_N}$, the more this eigenvalue moves towards the real number line. The other oscillatory eigenvalues in Fig. 9c are not affected by changes to the $\mathrm{FCR_N}$ sharing. They are associated with internal states of the excitation systems (Excs) and turbogenerators (GTs).

It is important to remark that eigenvalue analyses rely on approximating a nonlinear system, which should be at the steady-state operating point of interest, to a time-invariant linear model [67]. The analyses performed in Section IV-B and in this section are inadequate for predicting system stability after large perturbations which excite nonlinear features, that force controllers to switch parameter sets, or that result in changes to the grid topology. Therefore, eigenvalue analyses cannot be employed to evaluate the transition period while the $\mathrm{FCR_D}$ are already activated and the $\mathrm{FCR_N}$ are not yet fully settled at their maximum contribution due to actuator

TABLE III: Scaled down PHIL and full size converter data.

Device	Quantity	Full-Scale Converter (SW PowerFactory)		Scaled-Down Converter (PHIL)	
ESSGC (ac side)	Apparent power	10 MVA	1 pu	14.3 kVA	1 pu
	Voltage	690 V	1 pu	115 V	1 pu
	Current	8367 A	1 pu	72 A	1 pu
ESSGC (dc side)	Voltage	1200 V		200 V	
	Current	8333 A		71.7 A	
ESSTR	Transformer ratio	11 kV / 690 V		400 V / 400 V	
	Short-circuit inductance (from LV)	12.1 µH	0.08 pu	316 µH	0.108 pu
	Short-circuit resistance (from LV)	238 µΩ	0.005 pu	49.37 mΩ	0.0535 pu
$ESSL_{ac}$	Main reactor inductance	25.8 µH	0.17 pu	500 µH	0.17 pu
	Main reactor resistance	952 µΩ	0.02 pu	20 mΩ (estimated)	0.0217 pu
$ESSC_{ac}$	Capacitance	3.343 mF	0.05 pu	50 µF	0.0145 pu
$ESSR_{ac}$	Damping resistance	18.16 mΩ (series)	0.381 pu	47 kΩ (parallel)	50 967 pu
$ESSC_{dc}$	Capacitance	69.4 mF	$H = 5\,\text{ms}^{\dagger}$	14 mF	$H = 19.5\,\text{ms}^{\dagger}$

$^{\dagger}H$ equals the energy in the capacitor at rated dc voltage divided by the converter rated apparent power.

delays. To enable the study of the dynamic response to large disturbances of the expanded FCR_I proposed in this paper, including the effects of nonlinearities as saturations and dead bands, a reduced-scale PHIL test setup is implemented. This setup is validated in Section VII and the response to a large disturbance which forces FCR_N and FCR_D to interact is shown in Section VIII.

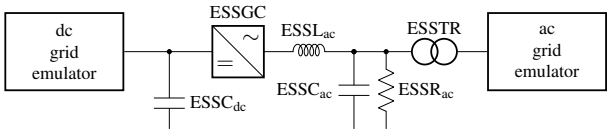

Fig. 11: Scaled-down PHIL test rig.

VII. Validation of the Power Hardware in the Loop Test Setup

In this section, the PowerFactory model used in Section VI is compared to a model running in a RTS [68] in a scaled-down PHIL test setup at the National Smart Grid Laboratory of NTNU, as seen in Fig. 10. This test setup is also employed later in Section VIII for comparing the performances obtained with the proposed extended FCR_I concept and with a state-of-the art technique employed in power-intensive isolated industrial grids. The hardware under test is composed of the ESSGC, dc link capacitance, and inductive-capacitive-inductive filter. These devices are marked with a dashed rectangle in Fig. 6 and their connections to the ac and dc grid emulator [69] are illustrated in Fig. 11. The ac grid emulator runs as a controlled voltage source and is connected to the high voltage side of ESSTR. The dc grid emulator runs as a controlled current source and feeds the dc link of the ESS with the net current coming from the ESDs. The scaling of the hardware under test is presented in Table III.

Three test cases are devised for the experimental results:

Case 1 – FCR_N provided only by the GTs;
Case 2 – FCR_N shared between BTC and GTs;
Case 3 – FCR_N shared between BTC and FLX.

For all cases: the total available FCR_N is $P_N = 3\,\text{MW}$, the FCR_D are provided only by the GTs, the boundary for normal and large disturbance operation is $\widetilde{f}_N = 1\,\text{Hz}$, and the total FCR_D gain is $6\,\text{MW/Hz}$ concentrated only in the GTs. The value of $\widetilde{f}_N$ represents $2\,\%$ of the rated system frequency, which is larger than the $0.2\,\%$ limit required for the Nordic region [19] but lower than $3\,\%$ defined for normal operation in the recommended practices for maritime vessels [37].

In this section, a step load of $3\,\text{MW}$ is chosen as test transient for comparing the scaled-down PHIL setup against the PowerFactory model. According to [9], this is the maximum expected load variation under normal operational conditions with $99.9\,\%$ of probability for the platform. The step load is divided between CPL and CZL proportionally to their rated values. For all three cases in this subsection, the FCR_N providers operate with a $0.25\,\%$ frequency dead band and their frequency-to-power gains are compensated with (4). It is worth remarking that, given the choices of P_N and $\widetilde{f}_N$, a step load of $3\,\text{MW}$ does not activate the large disturbance reserves.

The comparison of the PowerFactory model and the PHIL setup are shown in Fig. 12. The results obtained with power-hardware-in-the-loop are marked with "PHIL" and the ones obtained with PowerFactory are marked with "SW". Initially, the system is in steady state and the ELC is absorbing power (Fig. 12i). At $t = 10\,\text{s}$, the step load of $3\,\text{MW}$ is applied (Fig. 12e). The initial transient caused by the step load is noticeable at the busbar voltage (Fig. 12a) and at the total power supplied by the WF (Fig. 12c). The imbalance of power of $3\,\text{MW}$ is, initially, fully covered by the GTs (Fig. 12d) and causes the ac frequency to drop (Fig. 12b). When the FCR_N are shared between BTC and GTs (Case 2), the burden on the GTs is quickly halved. For Case 3, when the FCR_N are provided exclusively by the BTC and FLX, the power of the flexible loads (Fig. 12f) is reduced proportionally with the frequency deviation. This, together with the power delivered by the batteries (Fig. 12h), drives the generator power back to the level of before the step. The secondary frequency controller is activated at $t = 30\,\text{s}$. The ELC is quickly shut-down and the FCC (Fig. 12g) slowly starts to supply power regulating the frequency back to the nominal.

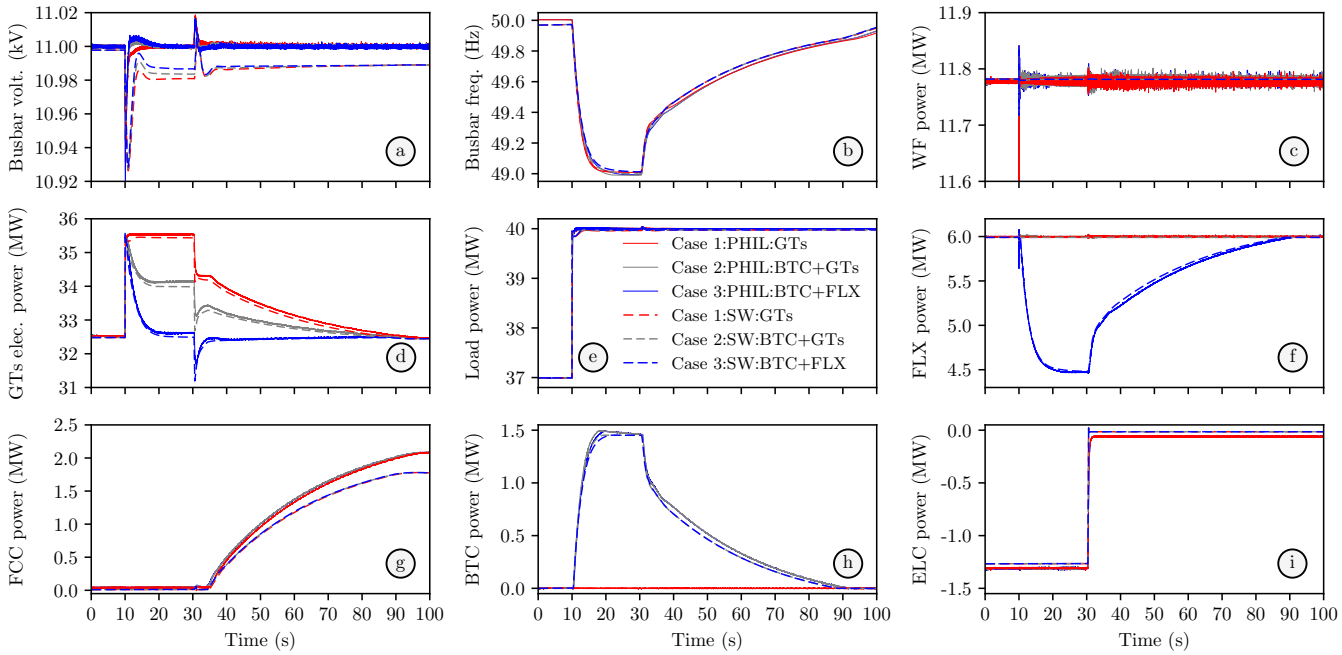

Fig. 12: Validation of the PHIL test bed with the PowerFactory model (marked as SW). Responses to 3 MW step loads with three different sharing of FCR_N. For clarity purposes, the WTs mechanical power is fixed and the action of the secondary controller after the frequency changes is delayed.

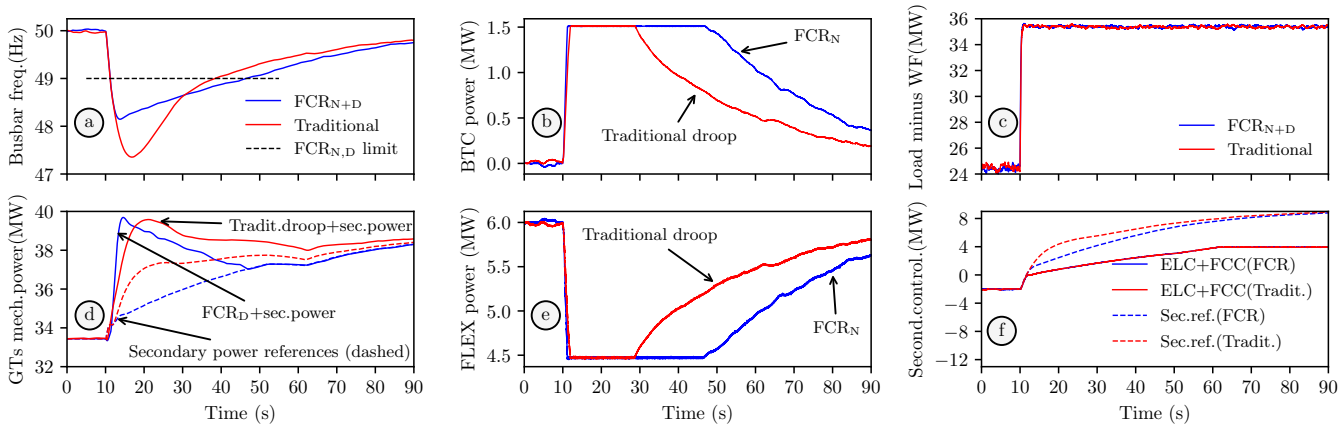

Fig. 13: Comparison between the extended FCR_I concept and the industry state-of-the-art droop. Responses to a loss of 11 MW production from the WF: FCR_{N+D} Case 3 in blue, traditional droop in red. The secondary controller responds to the frequency changes without intentional delays. Effects of wind turbulence in the power delivered by the WTs are considered.

VIII. Extended FCR_I versus Industry State-of-the-Art

In this section, the extended FCR_I concept is compared to the industry state-of-the-art droop with centralized secondary frequency controller. Case 3 from Section VII is selected for this benchmarking. The dead bands previously adopted for the FCR_N providers are now set to 10 mHz. For the traditional droop scenario, the total frequency-to-power gain of 3 MW/Hz is divided among the primary reserve providers in the following manner: 0.5 MW/Hz is assigned to each GT, 1 MW/Hz is assigned to the BTC, and the remaining 1 MW/Hz to the FLX. The turbulence effects on the WTs are now considered, see [9], [56].

Fig. 13 shows the comparison of the performance of the traditional droop method and the FCR_{N+D} Case 3. At $t = 10$ s, 11 MW of wind power production is lost, as seen in Fig. 13c. The PI regulator of the secondary power controller reacts to the frequency variation without intentional delays and changes the secondary power reference causing the ELC and FCC to respond (Fig. 13f). The difference between the required secondary power and the measured delivered power by the ELC and FCC is sent as reference to the GTs, as specified in (1). For that reason, the mechanical power delivered by the turbines to the synchronous generators (Fig. 13d) contains both the droop and the secondary power response. The FCR_{N+D} Case 3 prioritizes the BTC and FLX as providers in normal

operation. The $11\,\mathrm{MW}$ production loss leads those $\mathrm{FCR_N}$ providers to saturation (Fig. 13b,e) when the frequency crosses $49\,\mathrm{Hz}$ (Fig. 13a). A possible shortage of power caused by the saturation, however, is automatically covered by activation of the $\mathrm{FCR_D}$ from the GTs. By defining $\widetilde{f_\mathrm{N}}$ and calculating the gains K_N and K_D with (2) and (3), one ensures that an eventual saturation of the $\mathrm{FCR_N}$ providers is automatically covered by the activation of the $\mathrm{FCR_D}$.

IX. Discussion and Future Work

The main advantage of the extended $\mathrm{FCR_I}$ concept when compared to the traditional droop method is the flexibility provided for the selection of which units will be responsible for normal operation reserves and which ones will be responsible for the large disturbance reserves. Additionally, the proposed concept enables the choice of different frequency-to-power gains for the different operating conditions in isolated grids. It is also important to remark that the same provider can participate as both types of reserves depending on technical or economical reasons.

The provision of primary reserves by the faster ESS and FLX lessens the burden of the slower GTs with frequency control which leads to reduced wear and tear of the turbine governors, reduced NO_x and CO_2 emissions, and an improved overall electric power quality in the platform. Although the higher participation of the faster reserves results in a more damped response of the frequency after sudden load changes, there is a non-critical increase in the oscillations at the main busbar voltage. Therefore, interactions between the excitation system of the GTs and the reactive power control of the ESSGC need special attention. Additionally, the tuning of the ESS and FLX frequency measurement devices needs to be carefully performed as the oscillation modes associated with them move towards less damped regions of the complex plane when the contributions of these providers increase. Nevertheless, the eigenvalue analysis and dynamic simulations performed with PowerFactory and the results obtained with the PHIL test setup indicate that the benefits, from a grid stability perspective, outweigh the disadvantages of increasing the share of converter interfaced $\mathrm{FCR_N}$ reserves for primary frequency control in isolated grids.

As the total allocated reserve power is maintained by the PMS, a higher participation of the battery in the primary frequency control means a higher FCR gain in the BTC and a lower gain in the governors. This results in increased damping of an oscillation mode associated with governors and GTs, whereas oscillation modes associated with the BTC and battery main reactor (BTL) become less damped. While the reduction in damping of the BTC and BTL modes is not critical, as ζ is still larger than 0.87, the increased damping of governors and GTs modes is much more expressive, from $\zeta = 0.64$ to the real number line. Notwithstanding, there is a series of modes with ζ close to or lower than 0.5 which are associated with constant power devices as the fuel cell, electrolyzer, and WTs. Different tuning strategies for the controllers of these devices influence the location in the complex planes of these oscillation modes. However, an assessment of such tuning strategies is considered outside the scope of this paper and will be addressed in a future work.

There are a few discrepancies between the results obtained with the PHIL setup and the PowerFactory simulations. The most noticeable one is in the FCC power which is due to higher losses in the scaled-down hardware devices (denoted by ESSGC, $\mathrm{ESSL_{ac}}$, and ESSTR in Figs. 6 and 11) that are not present in the PowerFactory simulations. Normalized resistive losses in laboratory equipment as transformers, reactors, and converters tend to be higher than the normalized losses in their full-scale counterparts. A compromise between reducing losses and matching reactance and capacitance values in pu has to be made for a scaled-down PHIL test. This topic is addressed in more detail in [70].

X. Conclusion

In this paper, the Nordic synchronous system concept of islanded operation frequency containment reserves ($\mathrm{FCR_I}$) was expanded and subdivided into two categories. This strategy of categorized $\mathrm{FCR_I}$ was applied to the study case of an isolated complex industrial system which is fed by traditional GTs and by a WF, is dominated by CPLs, equipped with fast flexible CILs, and supported by an ESS. The analyses performed in this work took into consideration the detrimental effects of the CPLs and demonstrated that the overall stability of the system increased by shifting the primary power reserves from the slow GTs to the fast ESS and CILs. This also allowed the GTs of the study case to operate at a more constant power, which has the potential to reduce wear and tear in the turbine governors. While the reduction in the damping of oscillation modes associated with the CPLs and the PECs were not critical, the oscillation mode associated with the slow turbine governors were considerably damped when ESS and CIL reserves were prioritized. The results of this paper were supported by computer simulations, made publicly available, and PHIL tests. They demonstrate the versatility of the expanded $\mathrm{FCR_I}$ concept for coordinating fast primary power reserves in autonomous grids with increased participation of non-synchronous intermittent RESs.

Acknowledgment

This work was supported through the PETROSENTER scheme, under the "Research Centre for Low-Emission Technology for Petroleum Activities on the Norwegian Continental Shelf" (LowEmission), grant number 296207.

References

[1] "Emissions to Air," Norwegian Ministry of Petroleum and Energy (Olje- og Energidepartementet), Oslo, Norway, Report, 2023. [Online]. Available: https://www.norskpetroleum.no/en/environment-and-technology/emissions-to-air/

[2] "North Sea Transition Deal," Department for Business, Energy & Industrial Strategy, London, United Kingdom, Report NSTD, 2021. [Online]. Available: https://assets.publishing.service.gov.uk/government/uploads/system/uploads/attachment_data/file/972520/north-sea-transition-deal_A_FINAL.pdf

[3] A. S. Tamez and S. Dellaert, "Decarbonisation Options for the Dutch Offshore Natural Gas Industry," PBL Netherlands Environmental Assessment Agency and TNO Energy Transition, The Hague, Report PBL 416, 2020. [Online]. Available: https://www.pbl.nl/sites/default/files/downloads/pbl-2020-decarbonisation-options-for-the-dutch-offshore-natural-gas-industry_4161.pdf

[4] "Hywind Tampen PUD del II - Konsekvensutredning," Equinor, Oslo, Norway, Impact Assessment Report PL050 - PL057 - PL089, Mar. 2019. [Online]. Available: https://cdn.sanity.io/files/h61q9gi9/global/59db109a1ab7991e6b7546ef9b161dcfa74ec514.pdf?hywind-tampen-pud-del-II-konsekvensutredning-mars-2019-equinor.pdf

[5] "First Power from Hywind Tampen," Equinor, Oslo, Norway, Press release, Nov. 2022. [Online]. Available: https://www.equinor.com/news/20221114-first-power-from-hywind-tampen

[6] H. G. Svendsen, M. Hadiya, E. V. Øyslebø, and K. Uhlen, "Integration of Offshore Wind Farm with Multiple Oil and Gas Platforms," in *2011 IEEE Trondheim PowerTech*, Jun. 2011.

[7] A. R. Årdal, T. Undeland, and K. Sharifabadi, "Voltage and Frequency Control in Offshore Wind Turbines Connected to Isolated Oil Platform Power Systems," *Energy Procedia*, vol. 24, Jan. 2012.

[8] A. R. Årdal, K. Sharifabadi, O. Bergvoll, and V. Berge, "Challenges with Integration and Operation of Offshore Oil & Gas Platforms Connected to an Offshore Wind Power Plant," in *2014 Petroleum and Chemical Industry Conference Europe*, Jun. 2014.

[9] E. Alves, D. d. S. Mota, and E. Tedeschi, "Sizing of Hybrid Energy Storage Systems for Inertial and Primary Frequency Control," *Frontiers Energy Research*, vol. 9, May 2021.

[10] D. d. S. Mota, E. F. Alves, S. Sanchez-Acevedo, H. G. Svendsen, and E. Tedeschi, "Offshore Wind Farms and Isolated Oil and Gas Platforms: Perspectives and Possibilities," in *ASME 2022 41st International Conference on Ocean, Offshore & Arctic Engineering (OMAE)*. Hamburg, Germany: ASME, 2022.

[11] T. J. Zhong, I. L. Hong Lim, and J. Yang, "Energy Management Strategy Designed for Offshore Oil Rig with Offshore Wind," in *2022 IEEE 16th International Conference on Compatibility, Power Electronics, and Power Engineering (CPE-POWERENG)*, Jun. 2022.

[12] T. Zhou and B. Francois, "Energy Management and Power Control of a Hybrid Active Wind Generator for Distributed Power Generation and Grid Integration," *IEEE Transactions on Industrial Electronics*, vol. 58, no. 1, 2011.

[13] H. Devold, "Oil and Gas Production Handbook, an Introduction to Oil and Gas Production, Transport, Refining and Petrochemical Industry," ABB Oil and Gas, Oslo, Norway, Handbook Edition 3.0, Aug. 2013, ISBN 978-82-997886-3-2. [Online]. Available: https://library.e.abb.com/public/34d5b70e18f7d6c8c1257be500438ac3/Oil%20and%20gas%20production%20handbook%20ed3x0_web.pdf

[14] S. Sanchez, E. Tedeschi, J. Silva, M. Jafar, and A. Marichalar, "Smart Load Management of Water Injection Systems in Offshore Oil and Gas Platforms Integrating Wind Power," *IET Renewable Power Generation*, vol. 11, no. 9, pp. 1153–1162, Jul. 2017.

[15] "WIN WIN Joint Industry Project: Wind-Powered Water Injection," DNV GL AS, Høvik, Norway, Public Report, May 2019. [Online]. Available: https://www.dnv.com/news/making-wind-powered-water-injection-a-commercial-reality-148049

[16] K. S. Khan, I. V. M. dos Santos, G. B. dos Santos, M. B. C. Salles, and R. M. Monaro, "Evaluation of Deep-Water Floating Wind Turbine to Power an Isolated Water Injection System," in *ASME 2021 3rd International Offshore Wind Technical Conference*. ASME, Apr. 2021. [Online]. Available: https://asmedigitalcollection.asme.org/OMAE/proceedings/IOWTC2021/84768/V001T01A002/1107746

[17] E. Ela, M. Milligan, and B. Kirby, "Operating Reserves and Variable Generation," National Renewable Energy Lab. (NREL), Golden, USA, Technical Report NREL/TP-5500-51978, Aug. 2011. [Online]. Available: https://www.osti.gov/biblio/1023095

[18] "Establishing a Guideline on Electricity Transmission System Operation," European Union, Commission Regulation 2017/1485, Aug. 2017. [Online]. Available: https://eur-lex.europa.eu/legal-content/EN/TXT/?uri=CELEX%3A32017R1485&qid=1659510543956

[19] "Technical Requirements for Frequency Containment Reserve Provision in the Nordic Synchronous Area," ENTSO-E, Brussels, Belgium, Grid Code Version Pending Approval of Legal Methodology, Jun. 2022. [Online]. Available: https://www.statnett.no/globalassets/for-aktorer-i-kraftsystemet/marked/reservemarkeder/fcr-technical-requirements-2022-06-27.pdf

[20] P. Hasanpor Divshali and C. Evens, "Optimum Operation of Battery Storage System in Frequency Containment Reserves Markets," *IEEE Transactions on Smart Grid*, vol. 11, no. 6, pp. 4906–4915, Nov. 2020.

[21] K. Poplavskaya and F. Leimgruber, "Analysis of the Swedish FCR-N Market Design - Effects of Transition to Marginal Pricing and Free Bidding," AIT Austrian Institute of Technology GmbH, Wien, Austria, Technical Report Commissioned by Svenska kraftnät, Jan. 2021. [Online]. Available: https://www.svk.se/contentassets/22a7164df5c2415d9c2a8f69c08498f8/svk_report_analysis_of_fcr-n_market_design.pdf

[22] N. Modig, R. Eriksson, P. Ruokolainen, J. N. Ødegård, S. Weizenegger, and T. D. Fechtenburg, "Overview of Frequency Control in the Nordic Power System," ENTSO-E, Brussels, Belgium, Technical Report, Mar. 2022. [Online]. Available: https://www.epressi.com/media/userfiles/107305/1648196866/overview-of-frequency-control-in-the-nordic-power-system-1.pdf

[23] "Funksjonalitet for Separatdriftsregulering/Deteksjon (FCR-I) og Dødbånd," Statnett AS, Oslo, Norway, TechnIcal Note Dokument ID: 2375815, Oct. 2018. [Online]. Available: https://www.statnett.no/globalassets/for-aktorer-i-kraftsystemet/systemansvaret/soknad-om-idriftsettelse-av-anlegg-fos--14/funksjonalitet-for-separatdriftsregulering-og-deteksjon.pdf

[24] G. Olson, "Paralleling Dissimilar Generators: Part 3 – Load Sharing Compatibility," Cummins Inc., White paper Power topic #9017, 2010. [Online]. Available: https://mart.cummins.com/imagelibrary/data/assetfiles/0056549.pdf

[25] A. Schuster, "DSLC-2 Digital Synchronizer and Load Control," Woodward GmbH, Stuttgart, Germany, Manual 37443J DSLC-2 - Rev. J, Feb. 2022. [Online]. Available: https://wss.woodward.com/manuals/PGC/DSLC_MSLC_series/DSLC-2/01_Technical_Manuals/37443J_TM-DSLC-2.pdf

[26] "EasYgen-3000XT Series Genset Control," Woodward GmbH, Stuttgart, Germany, Manual Release 2.13-0, Document ID: B37580, Revision L, Build 52604, Oct. 2022. [Online]. Available: https://wss.woodward.com/manuals/PGC/easYgen-3000XT_series/easYgen-3400XT-3500XT-P1/01_Technical_Manuals/B37580_TM_easYgen-3400-3500-XT-P1_L.pdf

[27] K. Gubba Ravikumar, B. Bosley, T. Clark, and J. Garcia, "Generation Control System: Using Isochronous Load-Sharing Principles with Gas and Steam Turbine Generators," *IEEE Industry Applications Magazine*, vol. 25, no. 2, Mar. 2019.

[28] J. Z. Tee, K. H. Tan, I. L. H. Lim, K. Zhou, and O. Anaya-Lara, "Integration of Offshore Wind with O&G Platforms with an Energy Storage System," in *2019 IEEE PES Innovative Smart Grid Technologies Europe (ISGT-Europe)*, Sep. 2019.

[29] D. Hu, X. Zhao, X. C., and J. W., "Impact of Wind Power on Stability of Offshore Platform Power Systems," in *2008 Third International Conference on Electric Utility Deregulation and Restructuring and Power Technologies*, Nanjing, China, Apr. 2008.

[30] A. R. Årdal, S. D'Arco, R. E. Torres-Olguin, T. Undeland, and K. Shrarifabadi, "Parametric Sensitivity of Transients in an Islanded System with an Offshore Wind Farm Connected to an Oil Platform," in *Proceedings of the 2011 14th European Conference on Power Electronics and Applications*. Birmingham, UK: IEEE, Aug. 2011. [Online]. Available: https://ieeexplore.ieee.org/document/6020683

[31] G. Delille, B. Francois, and G. Malarange, "Dynamic Frequency Control Support by Energy Storage to Reduce the Impact of Wind and Solar Generation on Isolated Power System's Inertia," *IEEE Transactions on Sustainable Energy*, vol. 3, no. 4, pp. 931–939, Oct. 2012.

[32] Y. Liu, W. Du, L. Xiao, H. Wang, and S. Bu, "Sizing Energy Storage Based on a Life-Cycle Saving Dispatch Strategy to Support Frequency Stability of an Isolated System with Wind Farms," *IEEE Access*, vol. 7, Nov. 2019.

[33] J.-Y. Kim, J.-H. Jeon, S.-K. Kim, C. Cho, J. H. Park, H.-M. Kim, and K.-Y. Nam, "Cooperative Control Strategy of Energy Storage System and Microsources for Stabilizing the Microgrid during Islanded Operation," *IEEE Transactions on Power Electronics*, vol. 25, pp. 3037–3048, Dec. 2010.

[34] T. Hosseinimehr, A. Ghosh, and F. Shahnia, "Cooperative Control of Battery Energy Storage Systems in Microgrids," *International Journal of Electrical Power & Energy Systems*, vol. 87, pp. 109–120, May 2017.

[35] L. A. Wong, V. K. Ramachandaramurthy, P. Taylor, J. Ekanayake, S. L. Walker, and S. Padmanaban, "Review on the Optimal Placement, Sizing and Control of an Energy Storage System in the Distribution Network," *Journal of Energy Storage*, vol. 21, pp. 489–504, Feb. 2019.

[36] M. Farrokhabadi, C. A. Cañizares, J. W. Simpson-Porco, E. Nasr, L. Fan, P. A. Mendoza-Araya, R. Tonkoski, U. Tamrakar, N. Hatziargyriou,

D. Lagos, R. W. Wies, M. Paolone, M. Liserre, L. Meegahapola, M. Kabalan, A. H. Hajimiragha, D. Peralta, M. A. Elizondo, K. P. Schneider, F. K. Tuffner, and J. Reilly, "Microgrid Stability Definitions, Analysis, and Examples," *IEEE Transactions on Power Systems*, vol. 35, no. 1, Jan. 2020.

[37] "IEEE Recommended Practice for Electrical Installations on Shipboard–Design," IEEE Industry Applications Society, New York, USA, IEEE Std 45.1-2017, Aug. 2017.

[38] R. Teodorescu, M. Liserre, and P. Rodriguez, *Grid Converters for Photovoltaic and Wind Power Systems | IEEE eBooks | IEEE Xplore*. Wiley-IEEE Press, Dec. 2010, ISBN 978-0-470-05751-3.

[39] R. N. Fard and E. Tedeschi, "Integration of Distributed Energy Resources into Offshore and Subsea Grids," *CPSS Transactions on Power Electronics and Applications*, vol. 3, no. 1, Mar. 2018.

[40] S. Luo, "A Review of Distributed Power Systems Part I: DC Distributed Power System," *IEEE Aerospace and Electronic Systems Magazine*, vol. 20, no. 8, Aug. 2005.

[41] A. Kwasinski and C. N. Onwuchekwa, "Dynamic Behavior and Stabilization of DC Microgrids with Instantaneous Constant-Power Loads," *IEEE Transactions on Power Electronics*, vol. 26, no. 3, Mar. 2011.

[42] D. P. Ariyasinghe and D. M. Vilathgamuwa, "Stability analysis of Microgrids with Constant Power Loads," in *2008 IEEE International Conference on Sustainable Energy Technologies*, Nov. 2008, pp. 279–284.

[43] N. Bottrell, M. Prodanovic, and T. C. Green, "Dynamic Stability of a Microgrid with an Active Load," *IEEE Transactions on Power Electronics*, vol. 28, no. 11, pp. 5107–5119, Nov. 2013.

[44] S. Singh, A. R. Gautam, and D. Fulwani, "Constant Power Loads and Their Effects in DC Distributed Power Systems: A Review," *Renewable and Sustainable Energy Reviews*, vol. 72, May 2017.

[45] E. Hossain, R. Perez, A. Nasiri, and R. Bayindir, "Stability Improvement of Microgrids in the Presence of Constant Power Loads," *International Journal of Electrical Power & Energy Systems*, vol. 96, Mar. 2018.

[46] N. Hatziargyriou, J. Milanovic, C. Rahmann, V. Ajjarapu, C. Canizares, I. Erlich, D. Hill, I. Hiskens, I. Kamwa, B. Pal, P. Pourbeik, J. Sanchez-Gasca, A. Stankovic, T. Van Cutsem, V. Vittal, and C. Vournas, "Definition and Classification of Power System Stability – Revisited & Extended," *IEEE Transactions on Power Systems*, vol. 36, no. 4, pp. 3271–3281, Jul. 2020.

[47] "IEC 61400-27-1:2015 Wind turbines - Part 27-1: Electrical simulation models - Wind turbines," International Electrotechnical Commission, Geneva, Switzerland, International Standard IEC 61400-27-1:2015, Feb. 2015.

[48] M. Korpås, L. Warland, W. He, and J. O. G. Tande, "A Case-Study on Offshore Wind Power Supply to Oil and Gas Rigs," *Energy Procedia*, vol. 24, pp. 18–26, Jan. 2012.

[49] L. Riboldi, E. F. Alves, M. Pilarczyk, E. Tedeschi, and L. O. Nord, "Optimal Design of a Hybrid Energy System for the Supply of Clean and Stable Energy to Offshore Installations," *Frontiers Energy Research*, vol. 8, Dec. 2020.

[50] J. Fang, H. Li, Y. Tang, and F. Blaabjerg, "On the Inertia of Future More-Electronics Power Systems," *IEEE Journal of Emerging and Selected Topics in Power Electronics*, vol. 7, no. 4, pp. 2130–2146, Dec. 2019.

[51] P. Kundur, N. J. Balu, and M. G. Lauby, *Power System Stability and Control*, ser. EPRI Power System Engineering Series. New York, USA: McGraw-Hill, 1994.

[52] J. Machowski, *Power System Dynamics: Stability and Control*, 2nd ed. Chichester, U.K.: Wiley, 2008.

[53] S. D'Arco and J. A. Suul, "Equivalence of Virtual Synchronous Machines and Frequency-Droops for Converter-Based MicroGrids," *IEEE Transactions on Smart Grid*, vol. 5, no. 1, Jan. 2014.

[54] P. Pourbeik, R. Boyer, K. Chan, G. Chown, J. Feltes, C. Grande-Moran, L. Gérin-Lajoie, F. Langenbacher, D. Leonard, L. Lima, L. Hajagos, L. Hannet, W. Hofbauer, F. Modau, M. Patel, S. Patterson, S. Sterpu, A. Schneider, and J. Undrill, "Dynamic Models for Turbine-Governors in Power System Studies," IEEE Power & Energy Society, Technical Report PES-TR1, Jan. 2013. [Online]. Available: https://site.ieee.org/fw-pes/files/2013/01/PES_TR1.pdf

[55] E. Alves, G. Bergna-Diaz, D. Brandao, and E. Tedeschi, "Sufficient Conditions for Robust Frequency Stability of AC Power Systems," *IEEE Transactions on Power Systems*, vol. 36, no. 3, May 2021.

[56] D. d. S. Mota. (2023, Aug.) Data Repository for Manuscript Submission to IEEE TPWRS. [Online]. Available: https://doi.org/10.5281/zenodo.7113316

[57] D. d. S. Mota and E. Tedeschi, "Understanding the Effects of Exponentially Decaying DC Currents on the Dual dq Control of Power Converters in Systems with High X/R," in *2021 IEEE 15th International Conference on Compatibility, Power Electronics and Power Engineering (CPE-POWERENG)*. Florence, Italy: IEEE, Jul. 2021. [Online]. Available: https://ieeexplore.ieee.org/document/9501204

[58] L. P. Kunjumuhammed, B. C. Pal, C. Oates, and K. J. Dyke, "Electrical Oscillations in Wind Farm Systems: Analysis and Insight Based on Detailed Modeling," *IEEE Transactions on Sustainable Energy*, vol. 7, no. 1, pp. 51–62, Jan. 2016.

[59] A. Ortega and F. Milano, "Stochastic Transient Stability Analysis of Transmission Systems with Inclusion of Energy Storage Devices," *IEEE Transactions on Power Systems*, vol. 33, no. 1, Jan. 2018.

[60] ——, "Generalized Model of VSC-Based Energy Storage Systems for Transient Stability Analysis," *IEEE Transactions on Power Systems*, vol. 31, no. 5, Sep. 2016.

[61] D. d. S. Mota. (2021, Feb.) Data Repository of the Manuscript Offshore Wind Farms and Isolated Oil and Gas Platforms. [Online]. Available: https://doi.org/10.5281/zenodo.6095756

[62] "PowerFactory 2020 User Manual," DIgSILENT GmbH, Gomaringen, Germany, PF2020 r6805, Jun. 2020. [Online]. Available: https://www.digsilent.de/

[63] "IEEE Recommended Practice for Excitation System Models for Power System Stability Studies," IEEE Power & Energy Society, Park Avenue New York, NY 10016-5997 USA, Standard IEEE Std 421.5™-2016 (Revision of IEEE Std 421.5-2005), Aug. 2016.

[64] F. Fröhr and F. Orttenburger, *Introduction to Electronic Control Engineering*. Berlin and München, Germany; London, UK: Siemens Aktiengesellschaft; Heyden & Son LTD., 1982.

[65] J. A. Suul, M. Molinas, L. Norum, and T. Undeland, "Tuning of Control Loops for Grid Connected Voltage Source Converters," in *2008 IEEE 2nd International Power and Energy Conference*, Dec. 2008.

[66] S. Golestan, J. M. Guerrero, and J. C. Vasquez, "Three-Phase PLLs: A Review of Recent Advances," *IEEE Transactions on Power Electronics*, vol. 32, no. 3, pp. 1894–1907, 2017.

[67] K. Ogata, *Modern Control Engineering*, 5th ed., ser. Prentice-Hall Electrical Engineering Series. Instrumentation and Controls Series. Boston, USA: Prentice-Hall, 2010.

[68] "OP4510 System Description," OPAL-RT TECHNOLOGIES, Montreal, Canada, Hardware Products Documentation, 2022. [Online]. Available: https://opal-rt.atlassian.net/wiki/spaces/PODLP/overview

[69] "COMPISO System Unit (CSU)," EGSTON Power Electronics GmbH, Klosterneuburg, Austria, Operator Manual CSU X00-XGAMPX, 2018. [Online]. Available: https://www.egstonpower.com

[70] D. D. S. Mota, J. K. Banda, A. A. Adeyemo, and E. Tedeschi, "Harmonic-Invariant Scaling Method for Power Electronic Converters in Power Hardware-in-the-Loop Test Beds," *IEEE Open Journal of Industry Applications*, vol. 4, pp. 139–148, 2023.

Daniel dos Santos Mota (Member, IEEE) received his Eng. and M.Sc. degrees in electrical engineering from the University of São Paulo, Brazil, in 2003 and 2010, respectively. He is currently working toward the Ph.D. degree in electric engineering with the Norwegian University of Science and Technology (NTNU), Trondheim, Norway.

From 2003 to 2020, he held several positions with the Voith Group in Brazil and Norway. During this period, he contributed, from the drawing board to site testing, to the development of different lines of programmable-logic-controller-based excitation systems of synchronous generators. He was also involved in the design, engineering, commissioning, and service of excitation systems for numerous power plants in different countries. His latest assignment within the Voith Group was at Trondheim, Norway, as an Area Sales Manager of automation systems for hydro power plants. Since 2023, he is a Research Scientist with the Energy Systems Department of SINTEF Energy Research, Trondheim. His research interests include control strategies for the stability guarantee of isolated grids with large contributions of renewable energy sources, voltage and reactive power control of synchronous generators, power system stabilizers, and infrastructure for the electrification of transport.

Erick F. Alves (Senior Member, IEEE) received the Eng. degree in energy and automation from the University of São Paulo, Brazil, in 2007, the M.Sc. degree in electrical engineering from the Arctic University of Norway, Narvik, Norway, in 2018, and the Ph.D. degree in electric power engineering from the Norwegian University of Science and Technology, Trondheim, Norway, in 2023.

With a rich background in the industry, Dr. Alves held various positions at the Voith Group and Statkraft between 2007 and 2022, contributing to the design, engineering, and commissioning of electrical and control systems for more than 50 renewable power plants across 18 countries. Since 2022, he has been a Senior Electrical Engineer at Hystar, focusing on the development of electrical and control systems for green hydrogen production. His research interests encompass a wide range of topics, including optimal control, energy storage systems, power electronics, and condition monitoring, and he has authored or coauthored more than 20 journals and conference papers in these fields. Dr. Alves is a member of the IEEE Standards Association, CIGRÉ, and held several positions (Chair, Vice-Chair, Treasurer) with the IEEE Power and Energy Chapter, Norway.

Salvatore D'Arco received the M.Sc. and Ph.D. degrees in electrical engineering from the University of Naples "Federico II," Naples, Italy, in 2002 and 2005, respectively.

From 2006 to 2007, he was a postdoctoral researcher at the University of South Carolina, Columbia, SC, USA. In 2008, he joined ASML, Veldhoven, the Netherlands, as a Power Electronics Designer, where he worked until 2010. From 2010 to 2012, he was a postdoctoral researcher in the Department of Electric Power Engineering at the Norwegian University of Science and Technology (NTNU), Trondheim, Norway. In 2012, he joined SINTEF Energy Research where he currently works as a Chief Research Scientist. He is the author of more than 100 scientific papers and is the holder of one patent. His main research activities are related to control and analysis of power-electronic conversion systems for power system applications, including real-time simulation and rapid prototyping of converter control systems.

Santiago Sanchez-Acevedo received the electrical power engineering and Master degrees from the Universidad Tecnológica de Pereira, Pereira, Colombia, in 2006 and 2008, respectively. In 2015, he received the Ph.D. degree in electric power engineering at the Norwegian University of Science and Technology (NTNU), Trondheim, Norway.

In 2016, he joined as Post-Doctoral Research Fellow at NTNU, where he worked on interoperability of high voltage DC transmission systems. Since 2019, he is with SINTEF Energy Research, Trondheim, as a Research Scientist, where he is involved in projects regarding power system stability, HVDC transmission systems, Laboratory analysis of digital substations, validation of cyber-physical power systems and cyber-security.

Elisabetta Tedeschi (Senior Member, IEEE) received the M.Sc. (Hons.) degree in electrical engineering and the Ph.D. degree in industrial engineering from the University of Padua, Padua, Italy, in 2005 and 2009, respectively.

From 2009 to 2011, she was a Postdoctoral Researcher with the Norwegian University of Science and Technology (NTNU), working on the grid integration of offshore renewable energies. She was a Researcher/Marie Curie Fellow with Tecnalia, Spain, from 2011 to 2013, where she worked as the Principal Investigator in the FP7-Sea2grid Project, related to the storage needs for the grid integration of wave energy converters. From 2013 to 2014, she was a Research Scientist with SINTEF Energy, and an Adjunct Associate Professor with NTNU. In 2014, she became a Full Professor within the offshore grid with NTNU. Since 2020, she has also been a Full Professor with the Department of Industrial Engineering, University of Trento, Trento, Italy. She has a core competence in the design and control of energy conversion and transmission and distribution systems, with a focus on offshore energy and power-quality issues. She has led and/or contributed to more than 15 national and international scientific projects and she has authored or coauthored two book chapters and more than 150 journals and conference papers in the field of marine energy and energy conversion systems.